Novel catalyst materials for the cathode side of MEAs suitable for transportation applications				
G.A. 303492				16.02.2016
Deliverable **D2.5**	WP2	**Theoretical design of cathode catalysts based on DFT-screening of new Pt and Pd alloys**		
Deliverable: Publication				
Description of Deliverable: Subsequent submission of a publication (one or several) of results from WP2				
PM for D2.5: 4	Nature: O	Dissemination Level: PU	Delivery Date: 31.12.2014	Lead Beneficiary: DTU

Objectives of Work

The objective of the work package was to provide a fast way of predicting highly active cathode catalyst concepts by means of Density Functional Theory (DFT) calculations.

Description of Work Done / Results

The first paper submitted within this WP was described in D2.3. It has in the meantime been published in ACS Catalysis 5 (2015) 6032-6040 under the new title "A comparison between the oxygen reduction reaction activity of Pd_5Ce and Pt_5Ce: the importance of crystal structure", authors: Vladimir Tripkovic, Jian Zheng, Gian Andrea Rizzi, Carla Marega, Christian Durante, Jan Rossmeisl and Gaetano Granozzi.

Now a second paper has been published in Science 352 (2016) 73, summarizing both theoretical and experimental results on Pt-rare earth alloys. The paper is attached to this deliverable, but is not open access.

Title: Tuning the activity of Pt alloy electrocatalysts by means of the lanthanide contraction

Authors: María Escudero-Escribano, Paolo Malacrida, Martin H. Hansen, Ulrik G. Vej-Hansen, Amado Velázquez-Palenzuela, Vladimir Tripkovic, Jakob Schiøtz, Jan Rossmeisl, Ifan E.L. Stephens, Ib Chorkendorff

that its concentration-dependent behavior and values correspond to a crystallization transition that is consistent with that found in other condensed matter systems (*28*). A thermal expansion of ~0.01°C^{-1} of the lattice (fig. S8) stems from the decrease of an average NLC elastic constant K and quadrupolar elastic forces as temperature increases (K decreases by a factor of ~3 when the composite is heated from room temperature to ~34°C) (*22*).

Nanorods can be electrically concentrated and ordered starting from dilute initial dispersions (fig. S9), similar to the crystallization of hard sphere–like colloids when subjected to electrophoretic or dielectrophoretic forces (*29*). The triclinic crystal order is facilitated by applying 300 to 900 mV to transparent electrodes on inner substrates of the cell, which is lower than the threshold voltage needed for NLC switching. In response to these dc fields, the positively charged nanorods slowly move toward a negative electrode as a result of electrophoresis and eventually form a crystal as their concentration uniformly increases (fig. S9). These low voltages also facilitate uniform alignment of crystalline nuclei and healing of defects; in addition, they induce a giant electrostriction of the triclinic lattice, with ~25% strain at fields of 0.03 V μm^{-1} (fig. S8B). Because NLC is switched at ~1 V (*9*, *21*), colloidal crystal lattice orientations can be reconfigured while following the rotation of the director, although these processes are slow and complex. Electric fields, confinement in thin cells (thicknesses ≤15 μm) that are incompatible with an integer number of primitive cells in the colloidal crystal, variations in nanorod concentrations that exceed the range accommodated by an equilibrium triclinic lattice, and temperature changes control the primitive cell parameters (table S1) and prompt the formation of defects ranging from edge dislocations (fig. S11) to vacancies and grain boundaries (*2*, *22*, *30*).

We have introduced a highly tunable and reconfigurable colloidal system with competing long-range elastic and electrostatic interactions that lead to triclinic pinacoidal lattices of orientationally ordered nanorods. This unexpected triclinic crystallization of semiconductor particles at packing factors <<1% shows potential for the self-assembly of a wide variety of mesostructured composites on device-relevant scales, which can be tuned by weak external stimuli such as low-voltage fields and very small temperature changes. The control of particle charging allowed for tuning of the triclinic lattice periodicity between 0.5 and 1.6 μm, a range which can be extended by tuning the strength of electrostatic interactions through doping or deionizing NLCs (*10*–*13*) or through using nematics with different properties. Considering that dipolar and other multipolar elastic colloidal interactions in NLCs can be introduced and guided by controlling the boundary conditions at particle surfaces, and given that the control of NLC elastic constants may alter the angular dependencies of these interactions (*22*), our study sets the stage for explorations of mesoscopic colloidal positional and orientational ordering that can enable the engineering of material properties through spontaneous ordering of nanoparticles.

REFERENCES AND NOTES

1. H. N. W. Lekkerkerker, R. Tuinier, *Colloids and the Depletion Interaction* (Springer Netherlands, 2011).
2. P. M. Chaikin, T. C. Lubensky, *Principles of Condensed Matter Physics* (Cambridge Univ. Press, 1995).
3. V. N. Manoharan, *Science* **349**, 1253751 (2015).
4. P. F. Damasceno, M. Engel, S. C. Glotzer, *Science* **337**, 453–457 (2012).
5. B. Senyuk *et al.*, *Nature* **493**, 200–205 (2013).
6. P. Poulin, H. Stark, T. C. Lubensky, D. A. Weitz, *Science* **275**, 1770–1773 (1997).
7. S. Sacanna, W. T. M. Irvine, P. M. Chaikin, D. J. Pine, *Nature* **464**, 575–578 (2010).
8. M. R. Jones *et al.*, *Nat. Mater.* **9**, 913–917 (2010).
9. Q. Liu, Y. Yuan, I. I. Smalyukh, *Nano Lett.* **14**, 4071–4077 (2014).
10. B. Liu *et al.*, *Nat. Commun.* **5**, 3092 (2014).
11. S. K. Sainis, J. W. Merrill, E. R. Dufresne, *Langmuir* **24**, 13334–13337 (2008).
12. A. Yethiraj, A. van Blaaderen, *Nature* **421**, 513–517 (2003).
13. M. F. Hsu, E. R. Dufresne, D. A. Weitz, *Langmuir* **21**, 4881–4887 (2005).
14. T. C. Lubensky, D. Pettey, N. Currier, H. Stark, *Phys. Rev. E* **57**, 610–625 (1998).
15. R. W. Ruhwandl, E. M. Terentjev, *Phys. Rev. E* **55**, 2958–2961 (1997).
16. S. Ramaswamy, R. Nityananda, V. A. Raghunathan, J. Prost, *Mol. Cryst. Liq. Sci. Technol. A* **288**, 175–180 (1996).
17. C. P. Lapointe, T. G. Mason, I. I. Smalyukh, *Science* **326**, 1083–1086 (2009).
18. J. C. Loudet, P. Barois, P. Poulin, *Nature* **407**, 611–613 (2000).
19. A. Nych *et al.*, *Nat. Commun.* **4**, 1489 (2013).
20. F. Wang *et al.*, *Nature* **463**, 1061–1065 (2010).
21. H. Mundoor, I. I. Smalyukh, *Small* **11**, 5572–5580 (2015).
22. Materials and methods are available as supplementary materials on *Science* Online.
23. N. Bogdan, F. Vetrone, G. A. Ozin, J. A. Capobianco, *Nano Lett.* **11**, 835–840 (2011).
24. D. E. Sands, *Introduction to Crystallography* (Dover Publications, 2012).
25. D. B. Conkey, R. P. Trivedi, S. R. P. Pavani, I. I. Smalyukh, R. Piestun, *Opt. Express* **19**, 3835–3842 (2011).
26. C. A. S. Batista, R. G. Larson, N. A. Kotov, *Science* **350**, 1242477 (2015).
27. V. D. Nguyen, S. Faber, Z. Hu, G. H. Wegdam, P. Schall, *Nat. Commun.* **4**, 1584 (2013).
28. R. W. Cahn, *Nature* **413**, 582–583 (2001).
29. R. C. Hayward, D. A. Saville, I. A. Aksay, *Nature* **404**, 56–59 (2000).
30. I. I. Smalyukh, O. D. Lavrentovich, *Phys. Rev. Lett.* **90**, 085503 (2003).

ACKNOWLEDGMENTS

This research was supported by the U.S. Department of Energy, Office of Basic Energy Sciences, Division of Materials Sciences and Engineering, under award ER46921, contract DE-SC0010305 with the University of Colorado–Boulder. We acknowledge the use of electron microscopy facility at the National Institute of Standards and Technology, Boulder, and thank A. Sanders for the help with imaging. We thank P. Ackerman, Q. Liu, T. Lee, and T. Lubensky for discussions.

SUPPLEMENTARY MATERIALS

www.sciencemag.org/content/352/6281/69/suppl/DC1
Materials and Methods
Figs. S1 to S11
Table S1
Movie S1
References (*31*–*39*)

14 December 2015; accepted 26 February 2016
10.1126/science.aaf0801

ELECTROCATALYSIS

Tuning the activity of Pt alloy electrocatalysts by means of the lanthanide contraction

María Escudero-Escribano,[1,2]* Paolo Malacrida,[1] Martin H. Hansen,[3,4] Ulrik G. Vej-Hansen,[1,3] Amado Velázquez-Palenzuela,[1] Vladimir Tripkovic,[3,5] Jakob Schiøtz,[1,3] Jan Rossmeisl,[3,4] Ifan E. L. Stephens,[1,6]* Ib Chorkendorff[1]*

The high platinum loadings required to compensate for the slow kinetics of the oxygen reduction reaction (ORR) impede the widespread uptake of low-temperature fuel cells in automotive vehicles. We have studied the ORR on eight platinum (Pt)–lanthanide and Pt-alkaline earth electrodes, Pt_5M, where M is lanthanum, cerium, samarium, gadolinium, terbium, dysprosium, thulium, or calcium. The materials are among the most active polycrystalline Pt-based catalysts reported, presenting activity enhancement by a factor of 3 to 6 over Pt. The active phase consists of a Pt overlayer formed by acid leaching. The ORR activity versus the bulk lattice parameter follows a high peaked "volcano" relation. We demonstrate how the lanthanide contraction can be used to control strain effects and tune the activity, stability, and reactivity of these materials.

To reduce the Pt loading at the cathode of polymer electrolyte membrane fuel cells (PEMFCs), researchers have intensively studied alloys of Pt with late transition metals such as Ni or Co as oxygen reduction reaction (ORR) electrocatalysts (*1*–*6*). Catalysts exhibiting even greater activity and stability could be designed through the identification of the descriptors that control the performance (*7*–*10*). One single descriptor controls ORR activity, the ΔE_{OH} binding energy, by way of a Sabatier volcano: An ΔE_{OH} ~0.1 eV weaker than Pt(111) yields the optimum value (*11*). Other indirect descriptors related to ΔE_{OH} include the d-band center (*12*), the Pt-Pt

Downloaded from http://science.sciencemag.org/ on July 5, 2016

interatomic distance (*4*) and the generalized coordination number (*8*). Stability is a multiparametric challenge, hence requiring several descriptors, such as the alloying energy E_a (*11*, *13*), and dissolution potential (*14*, *15*).

Our earlier studies identified alloys of Pt and rare earths, in particular Pt_xY and Pt_xGd, as active and stable catalysts for oxygen reduction, both in the bulk polycrystalline (*11*, *16*) and nanoparticle (NP) form (*17*, *18*). The exceptionally negative E_a of Pt–rare earth alloys should increase their resistance to degradation (*11*, *13*). In contrast, more commonly studied ORR alloys, such as Pt-Ni or Pt-Co, typically degrade in long-term tests via dealloying (*19*, *20*). Nevertheless, new forms of Pt-Ni–based catalysts achieve exceptional activity and stability during short-term accelerated degradation tests (*5*, *21*, *22*). Nonetheless, engendering long-term stability in fuel cells (*20*) may require materials that are inherently less prone to dealloying. Because the rare earth (e.g., Y or Gd) is unstable against dissolution, a Pt overlayer is formed on the surface, as shown on Fig. 1, A and B. We showed that on Pt_xGd and Pt_xY NPs, the bulk compressive strain correlated strongly with increased ORR activity; this result suggested that the bulk strain is imposed onto the Pt surface atoms, weakening ΔE_{OH} (*23*). These observations led us to conjecture that other Pt-lanthanide alloys, exhibiting more optimal levels of compression, would reach the peak of the Sabatier volcano. Here, we show how the decreased radius of the lanthanides with increased filling of the f-shell—i.e., the lanthanide contraction—provides us with a route to engineer such compression. We have systematically studied activity and stability trends of Pt_5La, Pt_5Ce, Pt_5Sm, Pt_5Gd, Pt_5Tb, Pt_5Dy, Pt_5Tm, and Pt_5Ca, using a combination of experiments and theory to explain our observations.

We evaluated the electrocatalytic properties of sputter-cleaned polycrystalline Pt_5M electrodes by rotating disk electrode (RDE) voltammetry in O_2-saturated 0.1 M $HClO_4$. We chose a Pt:M ratio of 5:1 because we could obtain a consistent series of alloys with the same structure, allowing for a systematic investigation. Furthermore, it corresponds to the phase that is most Pt-rich and stable (*16*). At 0.9 V, Pt_5Tb is the most active polycrystalline Pt-based catalyst reported. All of the materials exhibited activity enhancement by a factor of 3 to 6 over pure Pt (see figs. S5 and S6 and table S1 in the supplementary materials). The overall electrocatalytic ranking of ORR activity of polycrystalline Pt alloys is shown in fig. S6: $Pt_5Tb > Pt_5Gd \sim Pt_3Y > Pt_5Sm > Pt_5Ca \sim Pt_5Dy > Pt_5Tm > Pt_5Ce > Pt_5Y \sim Pt_5La >> Pt$ (*6*, *11*, *16*), demonstrating that these alloys accelerate the ORR more effectively than other polycrystalline Pt alloys. Pt_3Co and Pt_3Ni alloys prepared this way exhibited enhancement only by a factor of 2 (*12*, *24*). Accelerated stability tests consisting of 10,000 consecutive cycles between 0.6 and 1.0 V versus a reversible hydrogen electrode (RHE) were performed after the initial ORR activity measurements. The electrochemical experiments are summarized in figs. S3 to S11. Figure 1C reports the ORR activities before and after the stability test for all the Pt alloys and pure Pt. Apart from Pt_5Ca (which has a lower E_a), all of the Pt-lanthanide alloys retained enhancement by a factor of 3 over pure Pt after the accelerated stability test. Notably, Pt_5Gd exhibited a residual activity that was 5 times as great as that of pure Pt.

We characterized the structure and chemical composition of the electrocatalysts by x-ray diffraction (XRD) and x-ray photoelectron spectroscopy (XPS) in order to explain our experimental observations. All of the alloys formed stable intermetallic compounds with a hexagonal structure (figs. S1 and S2 and table S1), in agreement with previous reports (*25*). The XRD data suggest that the polycrystalline alloys may show different degrees of preferential orientation in the bulk (figs. S1 and S2). However, by presputtering the electrodes, we minimize any differences in surface orientation between the samples under investigation. Moreover, based on Watanabe and coworkers' in situ scanning tunneling microscopy measurements on sputter-deposited Pt-Fe (*26*), we expect the acid-leached Pt overlayers to be dominated by (111) terraces, typically the most stable facet termination (*27*). Most of the elements in the bulk Pt_5M alloy form a so-called kagome layer (*6*, *16*) (Fig. 2 and fig. S16), with a nearest-neighbor Pt-Pt distance $d_{Pt\text{-}Pt} = a/2$. The lattice parameter a and hence $d_{Pt\text{-}Pt}$ decreased from left to right in the lanthanide series (Fig. 2).

Figure 3, A and B, show the angle-resolved XPS (AR-XPS) depth profiles on sputter-cleaned Pt_5Tb before and after electrochemical measurements. For each of the alloys, the Pt to M ratio increased substantially, especially at the most surface-sensitive angles, as shown for Pt_5Tb on Fig. 3C, after initial electrochemistry measurements, confirming the formation of a Pt overlayer. The depth profile of Fig. 3B showed that, even after accelerated stability tests, this structure was maintained, demonstrating the stability of these materials upon potential cycling.

To quantitatively interpret our XPS data (for details, see section S4 of the supplementary materials and figs. S12 to S15), we evaluated the mean Pt overlayer thickness for the alloys. Figure 3D shows how it varied for both the initial ORR activity and after stability tests as a function of the bulk lattice parameter a. The overlayer thickness after the initial testing varied little between the different alloys. However, after stability tests, the mean Pt overlayer generally increased from Pt_5La to Pt_5Tb [Pt_5Ca lies out of the scale; the initial Pt:M ratios for Pt_5Ca, Pt_5Sm, and Pt_5Dy were in fact higher than those expected from the nominal bulk stoichiometry (fig. S13), thus inhibiting a precise calculation of the overlayer thickness]. This difference could explain the anomalous behavior of

[1]Center for Individual Nanoparticle Functionality (CINF), Department of Physics, Technical University of Denmark, 2800 Lyngby, Denmark. [2]Department of Chemical Engineering, Stanford University, Stanford, CA 94305, USA. [3]Center for Atomic-Scale Materials Design (CAMD), Department of Physics, Technical University of Denmark, 2800 Lyngby, Denmark. [4]Nano-Science Center, Department of Chemistry, University of Copenhagen, 2100 Copenhagen, Denmark. [5]Department of Energy Conversion and Storage, Technical University of Denmark, 4000 Roskilde, Denmark. [6]Department of Mechanical Engineering, Massachusetts Institute of Technology, Cambridge, MA 02139, USA.
***Corresponding author. E-mail: ibchork@fysik.dtu.dk (I.C.); ifan@fysik.dtu.dk (I.E.L.S.); maria.escudero@fysik.dtu.dk (M.E.-E.)**

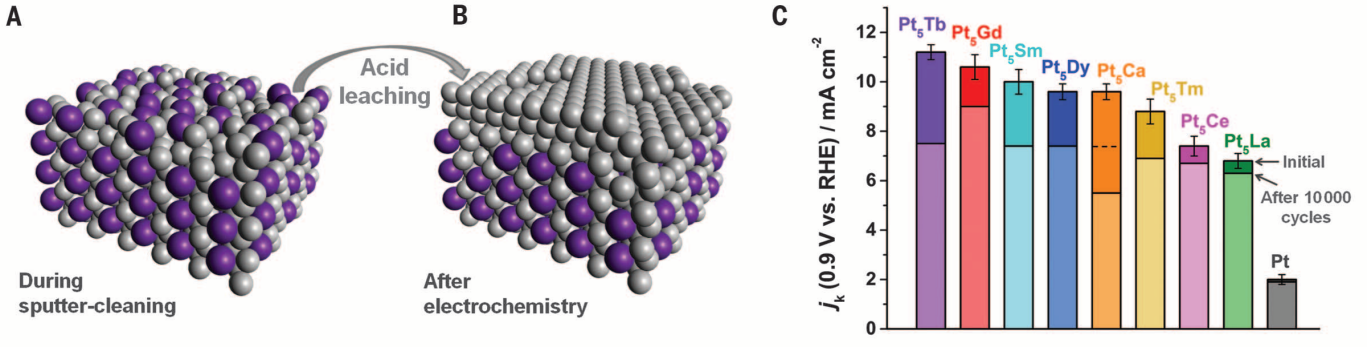

Fig. 1. Schematic views and electrochemical properties of polycrystalline Pt_5M (M = lanthanide or alkaline earth metal) electrocatalysts. Three-dimensional view of the Pt_5M structure (**A**) during sputter-cleaning and (**B**) after electrochemistry. (**C**) Kinetic current density, j_k, of Pt_5M and Pt at 23°C, 1600 revolutions per minute in O_2-saturated 0.1 M $HClO_4$, before and after a stability test consisting of 10,000 cycles between 0.6 and 1.0 V versus RHE at 100 mV s^{-1}. The activity of Pt_5Ca after the stability test has been normalized considering the increase of area after the test (see section S3.4 in the supplementary materials). The value normalized by the geometric area (dotted line) is shown for comparison.

Downloaded from http://science.sciencemag.org/ on July 5, 2016

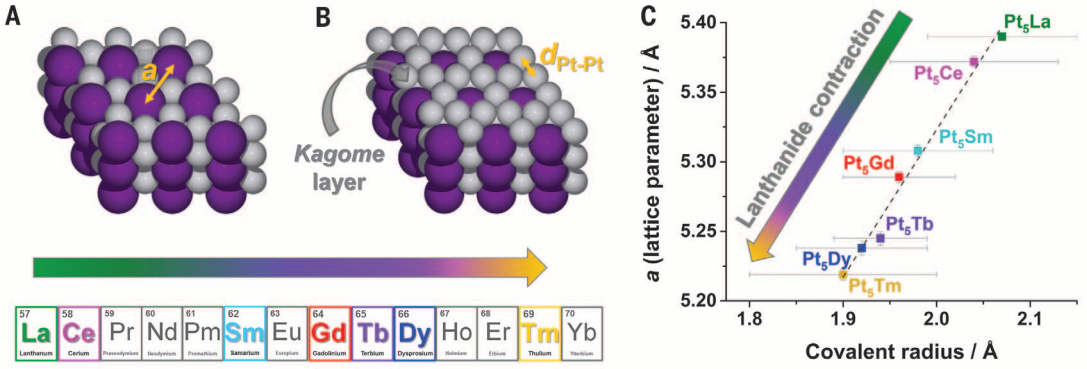

Fig. 2. Structure of Pt_5M. (**A** and **B**) Schematic view of the bulk structure of a Pt_5M (illustrated for Pt_5Tb), showing Pt_5Tb terminated by (A) a Pt and Tb intermixed layer and (B) a Pt kagome layer. Purple spheres represent Tb atoms, and gray spheres represent Pt atoms. Under ORR conditions in an acidic environment, one to two layers of M will be leached out, leaving three to five layers of Pt, as shown on Fig. 1B. (**C**) Relation between the lattice parameter *a* of Pt_5M measured by XRD (table S1) and the covalent radius of the lanthanide atoms (*31*). The dotted line shows the linear fit. The upper part of the figure shows the lanthanide contraction across the lanthanide series, the covalent radii decreasing in the same direction as d_{Pt-Pt}. The error in *a* corresponds to the uncertainty in the fit (table S1), whereas the error in the covalent radius corresponds to the estimated standard deviation from (*31*).

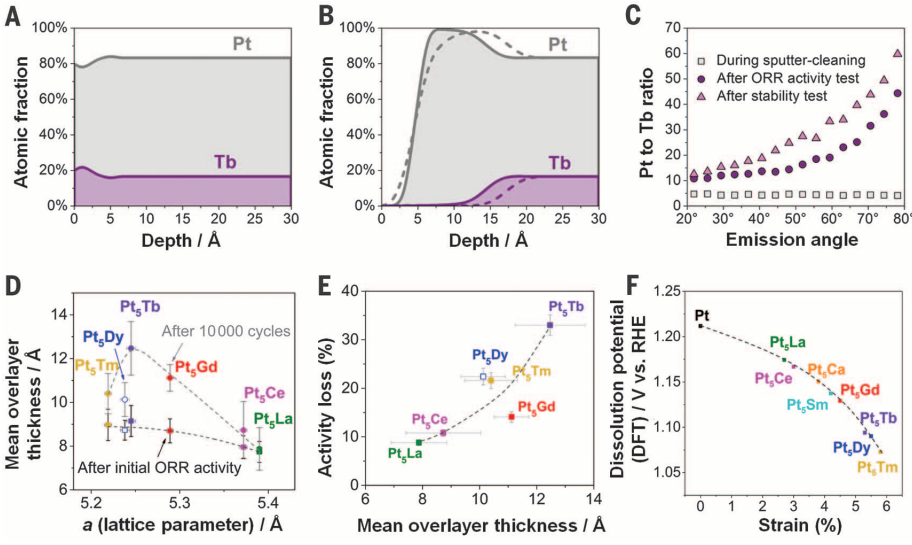

Fig. 3. XPS profiles before and after electrochemistry and Pt overlayer thickness as a function of the lattice parameter and activity loss. (**A and B**) AR-XPS profiles of polycrystalline Pt_5Tb (A) as prepared and (B) after initial ORR activity (solid line) and after stability test (dashed line). (**C**) Pt to Tb atomic ratios in Pt_5Tb from AR-XPS during sputter cleaning, after ORR initial activity, and after stability test. (**D**) Estimated average thicknesses of the Pt overlayer for Pt_5Tm, Pt_5Dy, Pt_5Tb, Pt_5Gd, Pt_5Ce, and Pt_5La after initial ORR activity and after stability test (taken from Fig. 1C), as a function of *a* lattice parameter [Pt_5Dy is shown as a hollow symbol to demarcate it as an outlier, likely because its as-prepared composition was inconsistent with that of the bulk (fig. S13)]. (**E**) Percentage of activity loss after stability test as a function of the Pt overlayer thickness. (**F**) Slab stability represented as dissolution potential versus the strain of the Pt overlayer on Pt_5M (from experimental lattice parameter *a*).

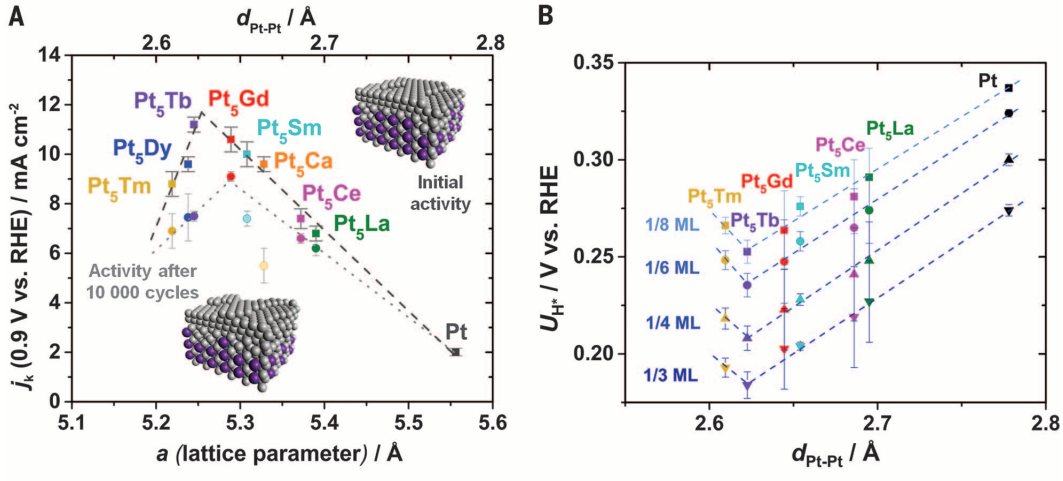

Fig. 4. Experimental volcano-type relationships between activity, H adsorption, and Pt-Pt distance. (**A**) Kinetic current density at 0.9 V (taken from Fig. 1C) on polycrystalline Pt_5M electrocatalysts versus the lattice parameter *a* of bulk Pt_5M (lower axis) and bulk d_{Pt-Pt} (upper axis), respectively. The figure shows the kinetic current density, j_k, of the alloys after the initial ORR activity (dark gray squares) and after 10,000 cycles of the stability test (colored circles). The dotted and dashed lines represent the experimental trends resulting after initial ORR activity and after stability, respectively. The activity of Pt_5Ca after 10,000 cycles has been normalized to account for the increase of area after the stability test. (**B**) Relation between the potential necessary to adsorb 1/8, 1/6, 1/4, and 1/3 monolayers (ML) of H (U_H) from the cyclic voltammograms (CVs) in the H adsorption region in N_2-saturated 0.1 M $HClO_4$ on Pt_5M (Fig. S5) and d_{Pt-Pt}.

Downloaded from http://science.sciencemag.org/ on July 5, 2016

these alloys, relative to the overall trend. The activity loss also correlates with the thickness of the overlayer (Fig. 3E) (*3*). Our density functional theory (DFT) calculations on the stability of different Pt overlayers, expressed as dissolution potential, show that the stability decreases as the compressive strain increases (Fig. 3F)—i.e., strain is a stability descriptor. We attribute the apparent thickening of the Pt overlayer with cycling to surface diffusion processes (*28*); bulk diffusion of lanthanide atoms through the overlayer will be strongly impeded by the strength of E_a (*13*). The strain-induced destabilization of the Pt overlayer could facilitate surface mobility (*28*), providing a channel for the dissolution of any residual lanthanide atoms in close vicinity to the surface. In summary, Fig. 3, D to F, shows that the overlayer thickness, activity losses, and thermodynamic stability are all a function of the bulk lattice parameter: Increased strain destabilizes the Pt overlayer and thus accelerates surface diffusion.

Figure 4A is a plot of the ORR activity as a function of the lattice parameter, a and $d_{Pt\text{-}Pt}$. Notably, all nine compounds, including the Pt-lanthanides and Pt_5Ca, follow the same volcano-type trend, with Pt_5Gd and Pt_5Tb at the apex. Because ΔE_{OH} is likely correlated with $d_{Pt\text{-}Pt}$ (*3*), the most trivial explanation for this trend is that the plot represents a Sabatier volcano: Alloys on the left bind OH too weakly, whereas on the right hand they bind ΔE_{OH} too strongly (as described by the DFT calculations in figs. S17 and S18). Alternatively, beyond a certain level of bulk strain, the overlayer could be unstable, causing the $d_{Pt\text{-}Pt}$ of the overlayer to relax toward a much lower level of surface strain. On single crystals, the destabilization is manifested as a positive shift in the "reversible" voltammetric peak for OH adsorption (*1*, *10*); however, we do not observe this shift on our polycrystalline materials, presumably because of hysteresis (electrochemical "irreversibility") or possibly coadsorption of OH and O. Conversely, the lanthanide contraction results in a clear voltammetric shift for the H adsorption region (figs. S3 and S4), plotted on Fig. 4B, which resembles the activity volcano, with Pt_5Tb exhibiting the maximum destabilization of adsorbed H. Notably, we also observe a linear relation between the experimental activity and the potential shift in the H adsorption (fig. S7).

Our DFT calculations on strain-activity-reactivity relations (section S5.4) suggest that Pt_5Tb, which is the most active electrocatalyst, should exhibit ~3% compression, approaching the optimum OH binding energy of the Sabatier volcano (*11*). By comparing our activity data and the voltammetric shift in H adsorption to the DFT predictions, we can conjecture that Pt-lanthanide alloys with a shorter $d_{Pt\text{-}Pt}$ than Pt_5Tb form a more relaxed overlayer (figs. S19 to S21]. More generally, our observations suggest that strain effects can only weaken the binding of H and OH to a certain extent. More appreciable destabilization of reaction intermediates can be afforded by ligand effects (*1*, *10*). The implementation of these catalysts in fuel cells will require scalable synthesis methods yielding high surface catalysts. Nonetheless, we have already demonstrated that Pt_xGd NPs exhibited an outstanding activity of 3.6 Å/mg Pt at 0.9 V RHE in liquid half cells (*18*, *29*) (fig. S6B), only surpassed by Pt_3Ni nanoframes (*21*) and Mo-doped Pt_3Ni nanoparticles (*22*). Careful tuning of the NP composition—for instance, by synthesizing ternary Pt-Gd-Tb alloys, in combination with a judicious choice of annealing treatment (*21*, *22*, *30*)—could yield record-breaking catalytic activity and stability over the long term in real devices.

REFERENCES AND NOTES

1. V. R. Stamenkovic *et al.*, *Science* **315**, 493–497 (2007).
2. H. A. Gasteiger, S. S. Kocha, B. Sompalli, F. T. Wagner, *Appl. Catal. B* **56**, 9–35 (2005).
3. P. Strasser *et al.*, *Nat. Chem.* **2**, 454–460 (2010).
4. S. Mukerjee, S. Srinivasan, M. P. Soriaga, J. McBreen, *J. Electrochem. Soc.* **142**, 1409–1422 (1995).
5. B. Han *et al.*, *Energy Environ. Sci.* **8**, 258–266 (2015).
6. I. E. L. Stephens, A. S. Bondarenko, U. Grønbjerg, J. Rossmeisl, I. Chorkendorff, *Energy Environ. Sci.* **5**, 6744 (2012).
7. J. K. Nørskov *et al.*, *J. Phys. Chem. B* **108**, 17886–17892 (2004).
8. F. Calle-Vallejo *et al.*, *Science* **350**, 185–189 (2015).
9. J. Suntivich, K. J. May, H. A. Gasteiger, J. B. Goodenough, Y. Shao-Horn, *Science* **334**, 1383–1385 (2011).
10. I. E. L. Stephens *et al.*, *J. Am. Chem. Soc.* **133**, 5485–5491 (2011).
11. J. Greeley *et al.*, *Nat. Chem.* **1**, 552–556 (2009).
12. V. R. Stamenkovic, B. S. Mun, K. J. J. Mayrhofer, P. N. Ross, N. M. Markovic, *J. Am. Chem. Soc.* **128**, 8813–8819 (2006).
13. U. G. Vej-Hansen, J. Rossmeisl, I. E. L. Stephens, J. Schiøtz, *Phys. Chem. Chem. Phys.* **18**, 3302–3307 (2016).
14. L. Tang *et al.*, *J. Am. Chem. Soc.* **132**, 596–600 (2010).
15. E. F. Holby, W. Sheng, Y. Shao-Horn, D. Morgan, *Energy Environ. Sci.* **2**, 865–871 (2009).
16. M. Escudero-Escribano *et al.*, *J. Am. Chem. Soc.* **134**, 16476–16479 (2012).
17. P. Hernandez-Fernandez *et al.*, *Nat. Chem.* **6**, 732–738 (2014).
18. A. Velázquez-Palenzuela *et al.*, *J. Catal.* **328**, 297–307 (2015).
19. K. J. J. Mayrhofer, K. Hartl, V. Juhart, M. Arenz, *J. Am. Chem. Soc.* **131**, 16348–16349 (2009).
20. L. Dubau *et al.*, *Appl. Catal. B* **142-143**, 801–808 (2013).
21. C. Chen *et al.*, *Science* **343**, 1339–1343 (2014).
22. X. Huang *et al.*, *Science* **348**, 1230–1234 (2015).
23. M. Mavrikakis, B. Hammer, J. K. Nørskov, *Phys. Rev. Lett.* **81**, 2819–2822 (1998).
24. V. Stamenkovic *et al.*, *Angew. Chem. Int. Ed.* **45**, 2897–2901 (2006).
25. V. Ohm *et al.*, *J. Alloy. C* **238**, 95–101 (1996).
26. L. J. Wan, T. Moriyama, M. Ito, H. Uchida, M. Watanabe, *Chem. Commun.* **2002**, 58–59 (2002).
27. L. Vitos, A. V. Ruban, H. L. Skriver, J. Kollar, *Surf. Sci.* **411**, 186–202 (1998).
28. J. Erlebacher, D. Margetis, *Phys. Rev. Lett.* **112**, 155505 (2014).
29. C. M. Pedersen *et al.*, *Electrochim. Acta* **179**, 647–657 (2015).
30. D. Wang *et al.*, *Nat. Mater.* **12**, 81–87 (2013).
31. B. Cordero *et al.*, *Dalton Trans.* **2008**, 2832–2838 (2008).

ACKNOWLEDGMENTS

The Center for Individual Nanoparticle Functionality is sponsored by the Danish National Research Foundation (DNRF54). We gratefully acknowledge EU FP7's initiative Fuel Cell and Hydrogen Joint Undertaking's project CathCat (GA 303492), as well as Danish Strategic Research's project NACORR (12-133817), for funding this work. M.E.-E. is the recipient of a Sapere Aude: DFF-Research Talent grant from the Danish Council for Independent Research. I.E.L.S. is the recipient of the Peabody Visiting Associate Professorship from the Department of Mechanical Engineering at Massachusetts Institute of Technology. We thank C. D. Damsgaard for assistance setting up the XRD measurements and O. Hansen for critically reading the manuscript. The authors declare competing financial interests: Intellectual property pertaining to the materials presented in this Report is protected by three patents (CA2877617-A1, WO2014079462-A1, and CA2767793-A1).

SUPPLEMENTARY MATERIALS

www.sciencemag.org/content/352/6281/73/suppl/DC1
Materials and Methods
Figs. S1 to S21
Table S1
References (*32*–*65*)

17 November 2015; accepted 11 February 2016
10.1126/science.aad8892

ICE SHEETS

Antarctic Ice Sheet variability across the Eocene-Oligocene boundary climate transition

Simone Galeotti,[1]* Robert DeConto,[2] Timothy Naish,[3,4] Paolo Stocchi,[5] Fabio Florindo,[6] Mark Pagani,[7] Peter Barrett,[3] Steven M. Bohaty,[8] Luca Lanci,[1] David Pollard,[9] Sonia Sandroni,[10] Franco M. Talarico,[10,11] James C. Zachos[12]

About 34 million years ago, Earth's climate cooled and an ice sheet formed on Antarctica as atmospheric carbon dioxide (CO_2) fell below ~750 parts per million (ppm). Sedimentary cycles from a drill core in the western Ross Sea provide direct evidence of orbitally controlled glacial cycles between 34 million and 31 million years ago. Initially, under atmospheric CO_2 levels of ≥600 ppm, a smaller Antarctic Ice Sheet (AIS), restricted to the terrestrial continent, was highly responsive to local insolation forcing. A more stable, continental-scale ice sheet calving at the coastline did not form until ~32.8 million years ago, coincident with the earliest time that atmospheric CO_2 levels fell below ~600 ppm. Our results provide insight into the potential of the AIS for threshold behavior and have implications for its sensitivity to atmospheric CO_2 concentrations above present-day levels.

The establishment of the Antarctic Ice Sheet (AIS) is associated with an approximate +1.5 per mil increase in deep-water marine oxygen isotopic ($\delta^{18}O$) values beginning at ~34 million years ago (Ma) and peaking at ~33.6 Ma (*1*–*3*), with two positive $\delta^{18}O$ steps separated by ~200,000 years. The first positive isotopic step primarily reflects a temperature decrease (*4*); the second isotopic step has been interpreted as the onset of a prolonged interval of

Downloaded from http://science.sciencemag.org/ on July 5, 2016

Tuning the activity of Pt alloy electrocatalysts by means of the lanthanide contraction
María Escudero-Escribano, Paolo Malacrida, Martin H. Hansen, Ulrik G. Vej-Hansen, Amado Velázquez-Palenzuela, Vladimir Tripkovic, Jakob Schiøtz, Jan Rossmeisl, Ifan E. L. Stephens and Ib Chorkendorff (March 31, 2016)
Science **352** (6281), 73-76. [doi: 10.1126/science.aad8892]

Editor's Summary

A lanthanide boost for platinum

High loadings of precious platinum are needed for automotive fuel cells, because the kinetics of the oxygen reduction reaction (ORR) are relatively slow. Escudero-Escribano *et al*. studied a series of platinum alloys with lanthanides and alkaline earth elements. When the surfaces were leached to leave pure platinum, they developed compressive strain that boosted the ORR activity—up to a factor of 6 for terbium. Enthalpy effects helped to stabilize these alloys under operating conditions.

Science, this issue p. 73

This copy is for your personal, non-commercial use only.

Article Tools Visit the online version of this article to access the personalization and article tools:
http://science.sciencemag.org/content/352/6281/73

Permissions Obtain information about reproducing this article:
http://www.sciencemag.org/about/permissions.dtl

Science (print ISSN 0036-8075; online ISSN 1095-9203) is published weekly, except the last week in December, by the American Association for the Advancement of Science, 1200 New York Avenue NW, Washington, DC 20005. Copyright 2016 by the American Association for the Advancement of Science; all rights reserved. The title *Science* is a registered trademark of AAAS.

Downloaded from http://science.sciencemag.org/ on July 5, 2016